Relaxing the alignment and fabrication tolerances of thin annular folded imaging systems using wavefront coding

Eric J. Tremblay,[1,*] Joel Rutkowski,[2] Inga Tamayo,[2] Paulo E. X. Silveira,[2] Ronald A. Stack,[3] Rick L. Morrison,[3] Mark A. Neifeld,[4] Yeshaiyahu Fainman,[1] and Joseph E. Ford[1]

[1]Department of Electrical and Computer Engineering, University of California San Diego, La Jolla, California 92093, USA
[2]CDM Optics, 4001 Discovery Dr., Suite 130, Boulder, Colorado 80303-7816, USA
[3]Distant Focus Corporation, Champaign, Illinois 61820-7460, USA
[4]Department of Electrical and Computer Engineering/College of Optical Sciences, University of Arizona, Tucson, Arizona 85721, USA

*Corresponding author: etremblay@ucsd.edu

Received 1 May 2007; accepted 15 June 2007;
posted 27 July 2007 (Doc. ID 82616); published 12 September 2007

Annular folded imagers can be up to 10× thinner than corresponding full-aperture imagers, but have tight fabrication tolerances and relatively shallow depth of focus. Wavefront coding, the use of specialized optics with postdetection signal processing, has been used to improve the depth of focus in full-aperture imaging systems. Here we explore the application of wavefront coding to annular folded optics. We compare the design and experimental results for an imaging system with a 38 mm focal length and just 5 mm total track. © 2007 Optical Society of America

OCIS codes: 080.2740, 110.4100, 100.2000, 220.1920.

1. Introduction

Ultrathin imaging systems have a variety of military and commercial applications due to their reduced weight and total track, allowing their ubiquitous use in aircraft and portable devices, for example. One method of achieving an extremely short total track consists of folding the optical system multiple times with multiple concentric reflectors, thus substituting free-space propagation with optical propagation inside the substrate of the imaging system [1,2]. Typically, the term "folded" refers to optical systems in which the optical axis is rotated through an angle (90° for example). In this case, folded describes 180° reflections back onto the same axis in the counterpropagating direction.

An ultrathin annular folded design with a large number of reflections requires the use of a large obscuration ratio (the ratio between the diameter of the central obscuration and the outer aperture diameter), which in turn requires a large entrance pupil diameter to achieve the same light-gathering capacity of an equivalent unobscured and unfolded optical design. Moreover, the multiple reflections required by the annular folded design increase the manufacturing sensitivity of the imaging system to certain fabrication tolerances, especially the total thickness of the substrate. Finally, the thin folded geometry and large entrance pupil diameter result in steep marginal ray angles at the focal plane. This creates an extremely shallow depth of focus [3]. This paper discusses the use of wavefront coding to alleviate these effects by increasing the fabrication tolerances while simultaneously extending the depth of focus of an annular folded imaging system. Wavefront coding reduces these problems by providing the system designer with the ability to trade off best focus performance for more tolerance to optical aberrations. This increased tolerance then can be budgeted to relax the alignment or fabrication tolerances or to extend the system's tolerance to optical aberrations such as defocus.

Wavefront coding uses a combination of specialized aspheric optical elements with postdetection signal processing to create a digital imaging system that is

0003-6935/07/276751-08$15.00/0

capable of producing acceptable image quality over a wider range of operating conditions than would be otherwise possible [4,5]. The specialized optical elements are designed to maximize the transfer of information in the presence of fabrication tolerances and aberrations (for example, defocus) rather than producing diffraction-limited images at best focus with a tight range of tolerances [6]. The images captured by these specialized elements (the wavefront-coded images) are then digitally processed to produce the final image.

Wavefront coding, as originally introduced by Dowski and Cathey [5], made use of a cubic-phase pupil function to render the optical transfer function (OTF) of an imaging system invariant to defocus. In recent years more general phase masks have been synthesized using a variety of design methods and optimization metrics. In addition to design in the frequency domain, several approaches for design in the spatial domain have been reported with metrics such as the point spread function (PSF), Strehl ratio, or information metrics used to optimize for defocus invariance [7–9]. In this paper we describe the application of wavefront coding to improve the fabrication and alignment tolerances of a high numerical aperture annular folded imaging system. We will also examine the improved depth of focus normally associated with wavefront-coded systems.

This paper is organized as follows: Section 2 presents a brief description of the annular folded imager, along with the design parameters, fabrication method, and tolerances. Section 3 describes the process of wavefront coding an annular folded imager, along with a description of the effects that an annular aperture has on spherical and coma aberrations. Section 4 presents some experimental results and a performance comparison between a wavefront-coded and a non-wavefront-coded system, and Section 5 concludes the paper.

2. Thin Annular Folded Design

A. Layout and System Specifications

Our objective in the design of an ultrathin imaging system was to create a visible-light color imaging system with 5 mm total track, light collection aperture area greater than or equivalent to that of a 25 mm unobscured imaging system, and resolution of at least 1000 × 700 pixels across a 0.1 rad field of view. To meet these specifications, an eight fold all-reflective design [2] was chosen and optimized in a commercially available ray-tracing program (Zemax). This design is shown schematically in Fig. 1.

The optimized annular folded design has a total track of 5 mm and a 60 mm outer diameter with an inner obscuration 53.5 mm in diameter. From the entrance aperture, light is focused by a series of eight reflections to the imaging plane in the central region of the optical element. Optical power and aberration correction are provided by four concentric aspheric reflectors on the back side of the element, arranged in a folded telephoto group where a strong positive-power reflector followed by a negative-power reflector help extend the focal length and enlarge the annular aperture. Since the optical path occurs within the calcium fluoride substrate the overall focal length of the imaging system is reduced by a factor of the index of refraction of calcium fluoride relative to an air-spaced folded design. The optical element was designed to be machined from a solid block of calcium fluoride using a diamond-tipped fast-tool servo. We chose calcium fluoride for its dimensional stability, low coefficient of thermal expansion, low optical dispersion, and especially for its compatibility with single-point diamond turning.

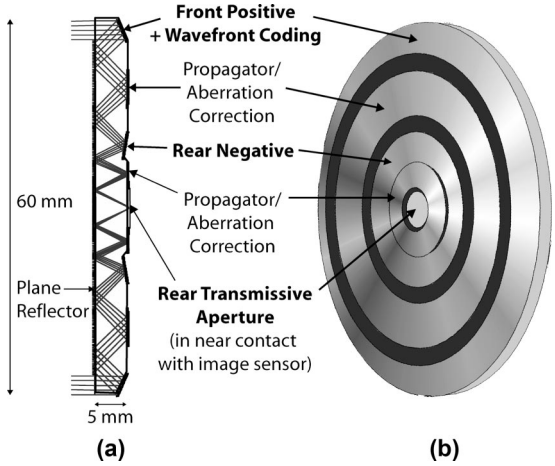

Fig. 1. Annular folded design. Zonal aspheric reflectors on the back side of the optical element focus light in an image sensor at the center of the element. (a) Cross section illustrating ray path. (b) Back (aspheric) side perspective view.

The optimized design has an effective aperture diameter of 27 mm, 38 mm effective focal length, and 0.12 rad of field of view, providing us with a resolution of 1280 × 960 pixels of an Omnivision 3620 complementary metal-oxide semiconductor (CMOS) color sensor. This sensor has 2048 × 1536 pixels with 3.18 μm pitch and was chosen for its small pixel pitch and high pixel count, of which a smaller subset is used. The number of concentric reflections and focal length were chosen to meet the resolution and pixel count requirements while taking into account the Omnivision sensor dimensions and the desired field of view. Although reflecting surfaces do not suffer from chromatic aberration, some aberration is present in the calcium fluoride substrate due to the refraction at the annular aperture. The annular folded design has ~8 μm of lateral color aberration over the full visible spectrum.

This imaging system is intended to be used as a fixed-focus camera of near-infinite (>200 m) object distance. To facilitate laboratory testing and demonstration of a prototype, the design was optimized for a fixed object distance of 2.5 m. The design also requires the use of index matching gel to fill a variable gap between the final transmissive surface of the calcium fluoride optical element and the sensor, and

to cancel the effect of the microlenses of the sensor array, which are not designed to operate with the large ray angles present in the design. This layer of gel between the optical element and the sensor array allows for a limited amount of focus adjustment. Good image quality can be obtained provided the gel layer is uniform and bubble-free.

B. Depth of Focus and Depth of Field

The folded reflective structure used in annular folded optics allows for dramatic reduction in overall thickness but also requires large marginal ray angles to allow for spatial separation of the reflective surfaces. These large marginal ray angles (image-plane numerical aperture of 0.7) allow for the resolution of the annular folded design to be sensor limited at the Nyquist frequency of the Omnivision CMOS sensor (156 cycles/mm) but also cause shallow depth of focus/depth of field. Without wavefront coding, the defocus tolerance for the annular folded design was estimated to be ± 5 μm (1.76 waves of defocus) for human viewing. This defocus tolerance maintains a modulation transfer function (MTF) of 20% at the sensor cutoff frequency across the full field and corresponds to a depth of field of only 24 mm at the designed object distance of 2.5 m. The depth of field improves considerably for larger object distances but is a limitation for imaging at close range.

C. Fabrication Tolerances

Since the optical element is fabricated from a single substrate with little assembly compensation possible, fabrication tolerances are inherently tight for the annular folded design. Once the optical element is fabricated, the only compensation available comes from the variable gap between the final transmissive surface and the sensor (focus adjustment). In addition, the folded optical path places an extremely tight tolerance on the thickness of the substrate since any error will be concatenated.

The nominal fabrication tolerances determined from a sensitivity analysis in Zemax for the annular folded design are shown in Table 1. Using focus position as the compensator, the tolerances given in Table 1 maintain an MTF greater than 20% at 156 cycles/mm across the full field. The range of focus compensation required is ± 28 μm.

D. Fabrication and Metrology

Single-point diamond turning in a fast-tool servo was chosen as the fabrication method due to its flexibility in shaping nonconventional aspheric surfaces in a large variety of substrates. Although all reflective, the folded optical element was chosen to be cut from a single calcium fluoride substrate to simplify fabrication. Compared to a hollow air-filled multiple-fold reflector, this optical element can be diamond turned without rechucking, which reduces centration errors in fabrication and alignment errors in assembly.

Surface metrology of large area, multiple zone aspheric optical elements is difficult due to its nonconventional shape and rapidly varying slopes. Conventional interferometric metrology relies on the comparison of the test surface with a reference surface (usually a sphere or a plane), and the phase difference is measured either in transmission or reflection. The folded optical element poses the challenges of (1) not possessing readily available reference nulls for each surface, making it difficult to measure the annular surface figures, and (2) presenting multiple high-powered annular surfaces, which are difficult to measure with a white-light profilometer (the oblique incidence angles require individual mechanical tilts and prevent accurate image stitching). Even if one could individually measure the figure of each surface, the challenge would lie on referencing the position of each surface vertex with respect to each other, and that (rather than the surface figure) is likely to be the main fabrication error and the strongest contributor to overall wavefront error.

Diamond turning technology, used primarily for fabricating high-quality infrared optics, can now produce good surface figure and acceptable surface roughness for visible-light optics. A representative aspheric surface profile in calcium fluoride measured using a large-magnification white-light interferometer (ADE Phase-shift MicroXAM) is shown in Fig. 2.

Table 1. Calculated Fabrication Tolerances for the Annular Folded Design

Description	Tolerances: Non-Wavefront Coded	Tolerances: Wavefront Coded
CaF_2 substrate thickness (nominal = 5 mm)	± 5 μm	± 10 μm
Departure from flat surface (front planar side)	0.25λ (546 nm)	0.25λ (546 nm)
Departure from aspheric surface equations	0.25λ (546 nm)	0.25λ (546 nm)
Zone shift, aspheric surface 1 (outermost)	± 15 μm	± 20 μm
Zone shift, aspheric surface 2	± 10 μm	± 10 μm
Zone shift, aspheric surface 3	± 10 μm	± 10 μm
Zone shift, aspheric surface 4 (innermost)	± 15 μm	± 20 μm
Zone tilt, aspheric surface 1 (outermost)	$\pm 0.010°$	$\pm 0.010°$
Zone tilt, aspheric surface 2	$\pm 0.010°$	$\pm 0.025°$
Zone tilt, aspheric surface 3	$\pm 0.020°$	$\pm 0.070°$
Zone tilt, aspheric surface 4 (innermost)	$\pm 0.030°$	$\pm 0.200°$

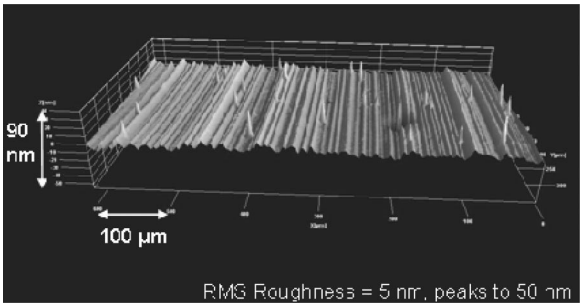

Fig. 2. Three-dimensional surface measurement of a diamond turned asphere in calcium fluoride using a large-magnification white-light interferometer.

This diamond turned surface shows an average roughness of 5 nm rms with peaks to 50 nm.

3. Wavefront Coding of an Annular Folded Design

The annular folded design was wavefront coded by reshaping the first reflective surface of the design, as shown in Fig. 1. This section starts with a description of the effects that a highly obscured folded imaging system has on spherical and coma aberrations, followed by a description of the wavefront-coded surface used in our design.

A. Aberration Mapping in Highly Obscured Annular Systems

The large obscuration ratio that is present in the annular folded design creates an interesting transformation of some typical third-order aberrations, namely, spherical aberration and coma more closely resemble defocus and tilt. This can be seen from the sets of rays displayed in Fig. 3.

A mathematical argument for aberration mapping can be made by evaluating the inner product of spherical aberration with defocus and the inner product of coma with tilt over the unit annulus. The fringe Zernike polynomial $Z_9 = 6r^4 - 6r^2 + 1$ represents spherical aberration and the fringe Zernike polynomial $Z_4 = 2r^2 - 1$ represents defocus. These two aberration functions can be compared using inner products over the unit annulus as given in Eq. (1):

$$\frac{\langle z_9,\, z_4\rangle}{\langle z_4,\, z_4\rangle} = \frac{\int_0^{2\pi}\int_a^1 Z_9 Z_4 r\,dr\,d\theta}{\int_0^{2\pi}\int_a^1 Z_4 Z_4 r\,dr\,d\theta} = \frac{3a^2 - 9a^4 + 9a^6}{1 - 2a^2 + 4a^4}. \quad (1)$$

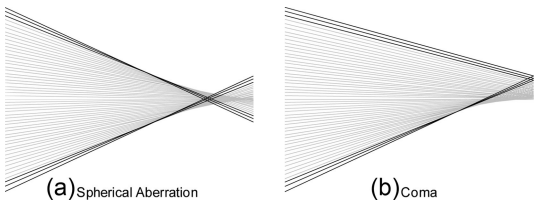

Fig. 3. Ray trace comparison of aberrations in a 90% obscured imaging system (dark lines) versus those in a conventional imaging system (gray lines). (a) Spherical aberration translates into defocus. (b) Coma translates into tilt.

Here the constant a represents the obscuration ratio of the system and can range from zero (no obscuration) to one (complete obscuration). At the extreme values of a two observations can be made. First, for a value of zero, Eq. (1) is zero, indicating that these two functions are orthogonal over the unit circle. This is a well-known property of Zernike polynomials [10,11]. However, in the limit where a approaches one, Eq. (1) is unity, indicating similarity between the functions. A similar analysis can be performed for coma and tilt. The fringe Zernike representation of coma is given by $Z_7 = (3r^3 - 2r)\cos(\theta)$ and $Z_2 = r\cos(\theta)$ for tilt. These two aberrations are compared in Eq. (2):

$$\frac{\langle z_7,\, z_2\rangle}{\langle z_2,\, z_2\rangle} = \frac{\int_0^{2\pi}\int_a^1 Z_7 Z_2 r\,dr\,d\theta}{\int_0^{2\pi}\int_a^1 Z_2 Z_2 r\,dr\,d\theta} = \frac{2a^4}{1 + a^2}. \quad (2)$$

Again, in the limit as a approaches one, Eq. (2) approaches unity, displaying the similarity between coma and tilt in the limit of extremely thin annuli.

B. Implications to Wavefront Coding Annular Systems

In general, wavefront-coded systems are designed to be invariant to defocus over a given operating range. On the other hand, certain aberrations, such as coma, tend to degrade the performance of such systems by reducing the modulation at all values of defocus. The aberration mapping described in Subsection 3.A makes the annular folded design form a particularly appealing candidate for wavefront coding in terms of the potential to correct for aberrations in the system because coma translates into simple tilt, no longer producing considerable degradation to the MTF. Likewise, spherical aberration translates into defocus, which is readily corrected for using wavefront coding. However, the thin annulus also poses a difficulty for applying wavefront coding. The thin annulus provides little opportunity for varying the exit pupil phase along the radial coordinate and, consequently, the selection of potential surface forms is limited. For the annular folded design, a well-suited surface is the so-called cosine-form, which has a small radially dependent component with a substantial cosinusoidally varying angular component [12]. Moreover, the cosine-form is readily suitable for diamond

turning using a fast-tool servo because the periodic shape of the surface is well mapped to the motion of the diamond tool. The general form of the cosine-form is described mathematically by

$$Sag_{\mathrm{WFC}}(r,\ \theta) = \sum_{i=1}^{m} a_i r^{bi} \cos(w_i\theta + \varphi_i), \qquad (3)$$

where r, θ, and Sag_{WFC} specify the surface position in cylindrical coordinates. The weight on each term is given by a_i and the radian frequency and phase are given by w_i and φ_i, respectively. In our annular design, the specific surface figure to be optimized is described by:

$$Sag_{\mathrm{WFC}}(r,\ \theta) = \sum_{i=1}^{m} a_i (10r - 9)^i \cos(3\theta) \quad \text{for } \{0.9 \le r \le 1.0\}. \qquad (4)$$

Typically, the wavefront-coded portion of the surface sag is added to the base curvature, conic, and aspheric portions of a surface at or near the aperture stop.

C. Wavefront-Coded Design and Nominal Performance

The annular folded design presented in Section 2 suffers from an extremely shallow depth of focus. This behavior is primarily due to the large numerical aperture of the unfolded, unobscured parent design. In the annular folded design a large diameter annular entrance pupil is required to achieve the equivalent light collection of a comparable unobscured system. Our primary goal was to apply wavefront coding to extend the depth of focus and therefore relax the alignment tolerance of the focal plane in tip, tilt, and axial position. Specifically, our goal was to maintain acceptable imaging performance over a depth of focus of ±10 μm.

To achieve this, a wavefront-coded surface as described in Eq. (4) was optimized with eight terms ($m = 8$). The wavefront-coded surface was first added to the folded design presented in Section 2. The previously described folded design was originally optimized using traditional lens design methods to have MTFs that were substantially close to each other as a function of field. The small variation of MTFs as a function of field is usually a requirement of successful wavefront-coded designs, since one expects to be able to use a single convolution kernel to deconvolve the whole image. A custom merit function was defined to optimize the filter and the wavefront-coded surface. The main goals of the merit function were: (1) to reduce the variation between MTFs as a function of field; (2) to reduce the amount of overshoot and undershoot of the MTFs after filtering; (3) to reduce the size of the filtered PSFs; and (4) to reduce the total amount of noise gain produced by the digital filter. We simultaneously optimized the wavefront-coded surface and the deconvolution filter using commercially available lens design software customized with our own merit function evaluation and filter design routines.

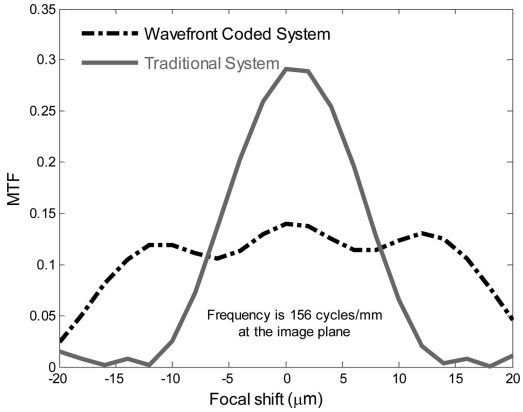

Fig. 4. Thru-focus MTF plot for an on-axis field point at 156 cycles/mm in image space, showing the expected extension of the depth of focus in the wavefront-coded design before filtering.

A plot showing the traditional and wavefront-coded thru-focus MTFs is shown in Fig. 4. In the wavefront-coded design, performance at the best-focus condition is sacrificed to maintain an acceptable performance over a larger depth of focus. In a wavefront-coded system, excess SNR at one operating point is traded to achieve acceptable performance throughout the entire operating range. The plot in Fig. 4 shows that our design has achieved a usable modulation of 12% within our design goal of ±10 μm (typically, a modulation greater than 10% is sufficient for good image restoration during the postprocessing step of a wavefront-coded system). The effect of the signal processing is best illustrated by examining the preprocessed and postprocessed point spread functions (PSFs). Thru-focus simulated digital PSFs for the wavefront-coded and traditional designs are presented in Fig. 5. The bottom row depicts PSFs for the case of traditional (non-wavefront-coded) imaging. The middle row depicts the preprocessed wavefront-coded PSFs, and the top row depicts the wavefront-coded PSFs after convolution with the digital filter shown in Fig. 6.

Note that the wavefront-coded PSFs have a threefold symmetry, resulting from the threefold symmetry of the pupil function. They also present a sharp, single-pixel central peak and symmetric legs that are about 4 pixels in length. After processing, the defocused wavefront-coded PSFs present a central peak that is sharper than the defocused traditional ones, with some noise surrounding the central peak. This means that we expect the wavefront-coded imaging system to yield sharper defocused images after processing with some added noise as a trade-off [12–14]. The noise penalty can be quantized by the noise gain of the digital filter used to reconstruct the wavefront-coded PSFs. This filter was synthesized using an adaptive matrix inversion algorithm, having a diffraction-limited reconstructed PSF as its optimization target. The synthesized 21 × 21 pixel filter shown in Fig. 6 has a noise gain of 1.35 for a 3 dB

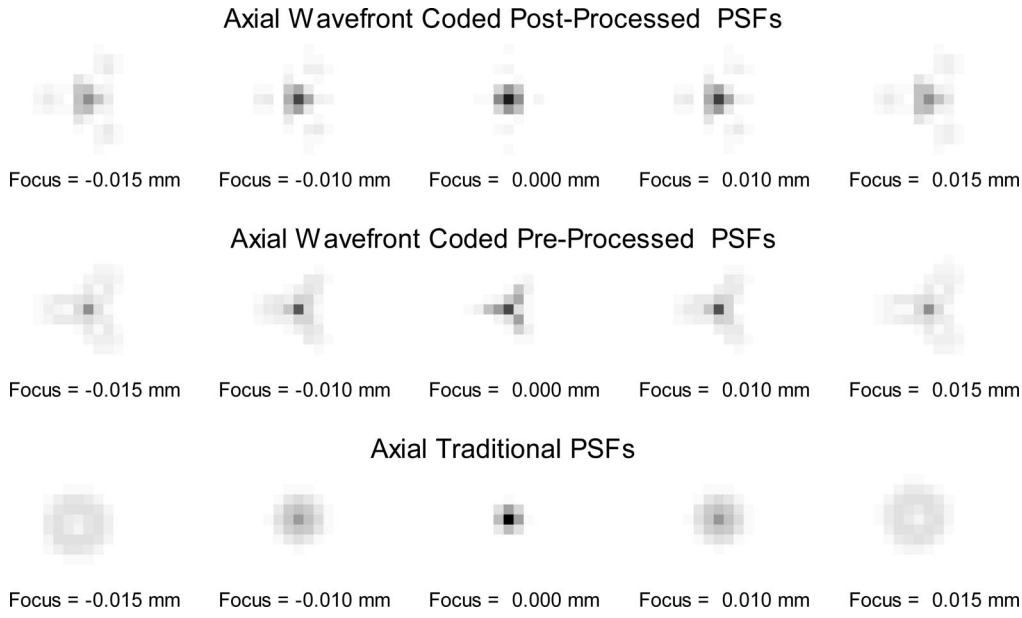

Fig. 5. Thru-focus simulated digital PSFs for the nominal wavefront-coded and traditional imagers.

bandwidth of 90% of the Nyquist frequency, meaning that we expect to recover almost the full resolution of the imaging system for a relatively small noise penalty. However, as will be shown in Section 4, the experimental results did not fully satisfy these expectations.

4. Experimental Results

This section presents the experimental results obtained using the wavefront-coded annular folded imager described in the previous sections and compares its performance to that of the non-wavefront-coded annular folded imager.

A. Measured Point-Spread Function

In the assembly of the wavefront-coded annular folded imager, it was necessary to align the optical element with respect to the rows and columns of the sensor array. This was done because of the circular asymmetry of the wavefront-coded pupil function and was necessary to allow us to use a convolutional decoding filter aligned with respect to the orientation of the PSF. The clear gel facilitates this alignment by allowing the calcium fluoride lens to be rotated while imaging a point source at the nominal object distance, positioned close to the center of the field of view. The correct orientation was found when one of the legs of the PSF was aligned with respect to one of the rows of the sensor array.

Figure 7 shows a PSF measured at the best-focus position after focus adjustment. The PSF was measured by imaging a 15 μm pinhole illuminated by a bright white-light source positioned 2.5 m away from the folded imager. The best-focus position then was found by varying the distance between the detector array and the folded imager using a micrometer. The position was varied until we found the most compact PSF possible.

As shown in the figure, the PSF is quite a bit larger than the predicted PSF. The central lobe alone is approximately 3×3 pixels wide and the size of each leg varies from 10 to 12 pixels wide. Moreover, the legs are uneven and asymmetric, showing quite a large discrepancy between the expected and measured PSFs. This discrepancy is mostly attributed to fabrication defects associated with wavefront coding

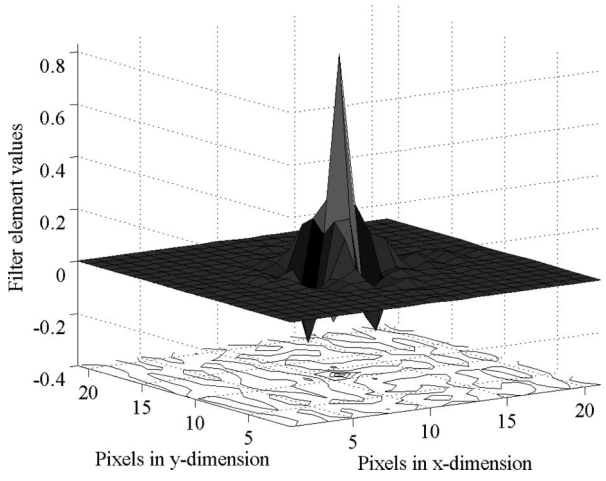

Fig. 6. Digital filter used to process wavefront-coded images. The noise gain is 1.35, meaning that a small noise penalty is expected.


Fig. 7. Best-focus PSF measured using wavefront-coded folded imaging system.

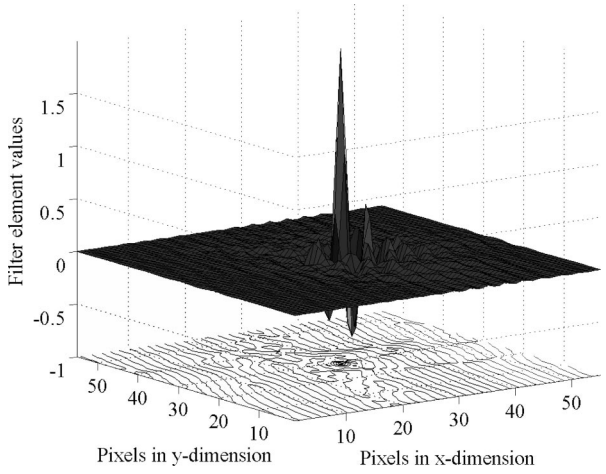

Fig. 8. Filter designed using measured PSF. The filter noise gain is 3.64, indicating that noisy images should be expected.

a design with tight tolerances and, as we will see, it negatively impacts the imaging quality of our system.

B. Filters

It is usually preferred to derive filters for decoding the wavefront-coded images using predicted PSFs. This is the case because the calculated PSFs are free from noise and aliasing, and the filters derived from them render good results when the fabricated parts are close to their respective designs. Unfortunately in this case the measured PSFs turned out to be considerably different from the expected ones, forcing us to use the measured PSFs in the synthesis of the filter. More than 30 different filters were produced using an adaptive matrix inversion algorithm, each filter slightly different in one or more of its design parameters (e.g., bandwidth, noise gain, tolerance to imaging artifacts, etc.). Then, each one of the filters was tested and a human observer selected the best filter, shown in Fig. 8. The filter is limited in size to 55×55 pixels (considerably large, to accommodate the large PSF). Its associated noise gain is 3.64 (quite large, meaning that noisy images should be expected as a result) and its maximum bandwidth is 87% of the Nyquist frequency (considerably large, in an attempt to recover as much detail as possible).

C. Performance Comparison

Figure 9 shows resolution targets at best-focus for (a) a non-wavefront-coded and (b) a wavefront-coded annular folded imaging system. Both images were captured using a resolution target placed 2.5 m away from the system. The color images were white balanced and then converted from raw to luminance-bandwidth-chrominance (YUV) images. We are showing the Y channel (luminance) only. In the case of the wavefront-coded image, the Y-channel information was convolved with the filter shown in Fig. 8 before producing the images shown.

At best focus the traditional and wavefront-coded imaging systems have nearly the same resolution ($\sim$1.587 line pairs per millimeter). However, one also

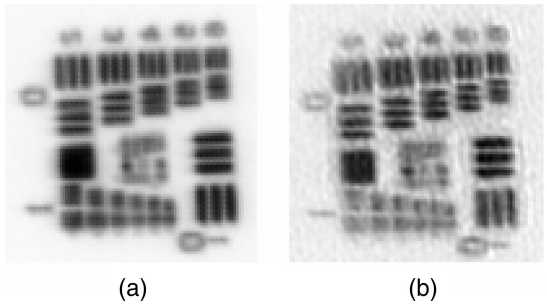

Fig. 9. U.S. Air Force (USAF) targets imaged through annular folded imagers at best-focus. (a) Non-wave-front-coded. (b) Wavefront-coded.

notices quite a bit of noise in the wavefront-coded image, which should be expected given the noise gain of the reconstruction filter.

Figure 10 shows the same bar targets imaged at the same distance away from the imager but this time the detector has been moved 10 μm away from the folded optical element, resulting in 3.53 waves of defocus. Note that the non-wavefront-coded image has lost some resolution, being now capable of resolving up to 1.414 line pairs per millimeter in the horizontal direction and $\sim$1.260 line pairs per millimeter in the vertical direction. The wavefront-coded image has also lost some resolution in the vertical dimension, but not in the horizontal dimension. It is now capable of resolving up to 1.414 line pairs per millimeter in the vertical dimension while maintaining 1.587 line pairs per millimeter of resolution in the horizontal dimension.

Thus, we see that fabrication defects provided us with PSFs that are quite a bit larger than expected. This forced us to use measured data to produce our decoding filters, and the resulting filters had high noise gains, resulting in noisy images. Nevertheless, we have shown that even under these unfavorable conditions wavefront coding was still capable of providing some advantage in imaging resolution over a non-wavefront-coded system. Future designs can be improved by: (1) using fabrication processes with tighter tolerances and (2) taking into account the sensitivity of the design to different tolerances (other than defocus) when designing the wavefront-coded

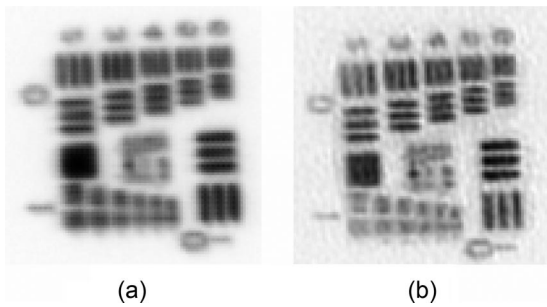

Fig. 10. USAF targets imaged through annular folded imagers at 10 μm away from best focus. (a) Non-wave-front-coded. (b) Wavefront-coded.

surface, that way further increasing the fabrication tolerance of the resulting wavefront-coded system.

5. Conclusions

We have discussed the use of wavefront coding for an annular folded imager, associating the considerable advantages of short total track and low total weight of an annular folded design with the ability to increase the depth of focus and to alleviate fabrication tolerances provided by wavefront coding. We also introduced the cosine form as a surface that is well suited to the design and fabrication of annular imaging systems. Unfortunately, the measured PSFs turned out to be considerably larger than the designed ones, forcing us to use high noise gain filters that had to be designed based on experimental PSFs. Even so, we showed that the wavefront-coded annular folded imaging system had the ability to resolve more detail over a large range of defocus than a non-wavefront-coded annular folded imaging system. We expect that applying similar techniques to a less radically folded lens system will yield significantly improved results.

The authors acknowledge Ravi Athale and Dennis Healy at Defense Advanced Research Projects Agency (DARPA) for many useful technical discussions; and Fresnel Technologies and ISP optics for fabrication services. This research was supported by DARPA via the MONTAGE program, grant HR0011-04-I-0045, and by the Natural Sciences and Engineering Research Council of Canada (NSERC) through a graduate student scholarship.

References

1. V. Draganov and D. G. James, "Compact telescope for free-space communications," in *Current Developments in Lens Design and Optical Engineering III,* Robert E. Fischer, Warren J. Smith, R. Barry Johnson, eds., Proc. SPIE **4767,** 151–158 (2002).
2. E. J. Tremblay, R. A. Stack, R. L. Morrison, and J. E. Ford, "Ultrathin cameras using annular folded optics," Appl. Opt. **46,** 463–471 (2007).
3. J. Hall, "F-number, numerical aperture, and depth of focus," in *Encyclopedia of Optical Engineering* (Dekker, 2003), pp. 556–559.
4. W. T. Cathey and E. Dowski, "A new paradigm for imaging systems," Appl. Opt. **41,** 6080–6092 (2002).
5. E. R. Dowski, Jr. and W. T. Cathey, "Extended depth of field through wavefront coding," Appl. Opt. **34,** 1859–1866 (1995).
6. K. Kubala, E. Dowski, J. Kobus, and R. Brown, "Aberration and error invariant space telescope systems," in *Novel Optical Systems Design and Optimization VII,* J. M. Sasian, R. J. Koshel, P. K. Manhart, and R. C. Juergens, eds., Proc. SPIE **5524,** 54–65 (2004).
7. W. Chi and N. George, "Electronic imaging using a logarithmic asphere," Opt. Lett. **26,** 875–877 (2001).
8. S. Prasad, T. C. Torgersen, V. P. Pauca, R. J. Plemmons, and J. van der Gracht, "Engineering the pupil phase to improve image quality," in *Visual Information Processing XII,* Z. Rahman, R. Schowengerdt, and S. Reichenbach, eds., Proc. SPIE **5108,** 1–12 (2003).
9. S. S. Sherif and W. T. Cathey, "Reduced depth of field in incoherent hybrid imaging systems," Appl. Opt. **41,** 6062–6074 (2002).
10. S. N. Bezdidko, "The use of Zernike polynomials in optics," Sov. J. Opt. Technol. **41,** 425–429 (1974).
11. A. B. Bhatia and E. Wolf, "On the circle polynomials of Zernike and related orthogonal sets," Proc. Cambridge Philos. Soc. **50,** 40–48 (1954).
12. K. Kubala, E. Dowski, and W. T. Cathey, "Reducing complexity in computational imaging systems," Opt. Express **11,** 2102–2108 (2003).
13. B. R. Frieden, "Image enhancement and restoration," in *Topics in Applied Physics,* Vol. 6 of *Picture Processing and Digital Filtering,* T. S. Huang, ed. (Springer-Verlag, 1979), pp. 177–248.
14. H. C. Andrews and B. R. Hunt, *Digital Image Restoration* (Prentice Hall, 1977), Chap. 8, pp. 147–152.